Supporting Information

Targeted Removal of Interfacial Adventitious Carbon towards Directional Charge Delivery to Isolated Metal Sites for Efficient Photocatalytic H_2 Production

Yunxiang Li, Shengyao Wang, Pei Wang, Yu He, Xusheng Wang, Kun Chang, Huiwen Lin, Xing Ding, Hao Chen, Hongwei Zhang, Yasuo Izumi, Tetsuya Kako and Jinhua Ye**

Contents

Supplemental experimental procedures

Chemicals: chemicals including melamine (99.0%), zinc acetate ($Zn(OAc)_2$), cobalt acetate tetrahydrate ($Co(CH_3COO)_2 \cdot 4H_2O$; 99%), iron(III) nitrate nonahydrate ($Fe(NO_3)_3 \cdot 9H_2O$; 99.9%), nickel chloride hexahydrate ($NiCl_2 \cdot 6H_2O$; 99.9%), methanol (99.5%), ethanol (99.5 %), lactic acid, sodium hydroxide (NaOH; 97%) and hydrochloric acid (HCl; 36%) were purchased from the Wako Co. and cadmium sulfide (CdS; 98%) was purchased form Strem Chemical, Inc. All of them were used without further purification.

Electrochemical measurements: The photoelectrochemical properties were investigated in a three-electrode cell by using an electrochemical station (Model-660D, CH instruments). The catalyst coated ITO glass, a Pt foil, and an Ag/AgCl electrode and lactic acid solution (20 vol % lactic acid, pH: 5.1) were used as the working electrode, the counter-electrode, the reference electrode, and the electrolyte, respectively. A 300 W Xe arc lamp equipped with a L42 cutoff filter was utilized as a light source ($\lambda > 400$ nm). EIS were recorded at an applied potential of -0.6 V versus Ag/AgCl over the frequency range of 0.1 MHz-0.1 Hz. The photocurrent with on/off cycles was measured at an applied potential of -0.6 V versus Ag/AgCl.

Computational details: Spin-polarized calculations were conducted with the Vienna Ab-initio Simulation Package (VASP 5.4.4).[1, 2] The electron exchange and correlation were described with the generalized gradient approximation (GGA) using Perdew–Burke–Ernzerhof (PBE) functional.[3] The electron-ion interaction was described by the projector augmented-wave formalism (PAW).[4, 5] Since GGA was not able to correctly describe the d electronic structure of the metal, the GGA+U approximation was adopted with the Dudarev ‘‘+U’’ term with a U-J value of 3 eV for the d electrons of Fe, Ni and Co atoms,[6, 7] since the U-J value chosen from 3.00 eV to 3.42 eV has merely influence for the H binding energy from our test results. The plane wave cut-off energy is set to 400 eV and electronic self-consistent convergence is 10^{-6} eV. Geometries were converged to a residual force smaller than 0.02 eV/Å. The Brillouin zone was integrated by a 3 × 3 × 1 Monkhorst–Pack grid. In the case of H_2 molecular, which was set in a 15×15×15 Å cubic box, the Gamma point only calculation was performed.

The CC model was built from 5×5 graphene (001) surface monolayer, which contains 50 atoms in total, and the vacuum thickness was set to 12 Å. To create the NC model, one of C atom was replaced by an N atom from the CC model. While the Fe-NC model was built by embedding a FeN_4 atomic structure in the CC model. During geometry optimization of CC model, NC model, and Fe-NC model, all atomic positions were fully relaxed and the lattice constant was relaxed in 2 dimensions, the optimized lattice parameters were listed in Table S1, and optimization structures were shown in Figure S18,19, 20. The Fe was replaced by Co, Ni, and vacancy, resulting in the Co-NC, Ni-NC and NC_{vac} model (Figure S18c and S18d), respectively. In order to compare the influence of metal, the lattice constant was consistent with the Fe-NC model. The H could adsorb on the C, N, and Metal (M) site of the surface, as shown in Figure S19 and Table S4.

The binding free energies of the H atom on surface were calculated via $\Delta G = G_{H/surf} - G_{surf} - 1/2G_{H2}$, where $G_{H/surf}$ denoted the free energy of H adsorbent model, G_{H2} represented the free energy of H_2 molecular and G_{surf} stood for the free energy of surface, including CC, NC, NC_{vac},

Fe-NC, Ni-NC, and Co-NC model. The free energy was obtained from the equation $G = E_{ele} + E_{vib} + E_t + E_r - TS$ as in our previous work,[8] where E_{ele}, E_t, E_r, and E_{vib} are the electronic, translational, rotational and vibrational energies, respectively. And S is the entropy, T was set to room temperature (298.15 K).

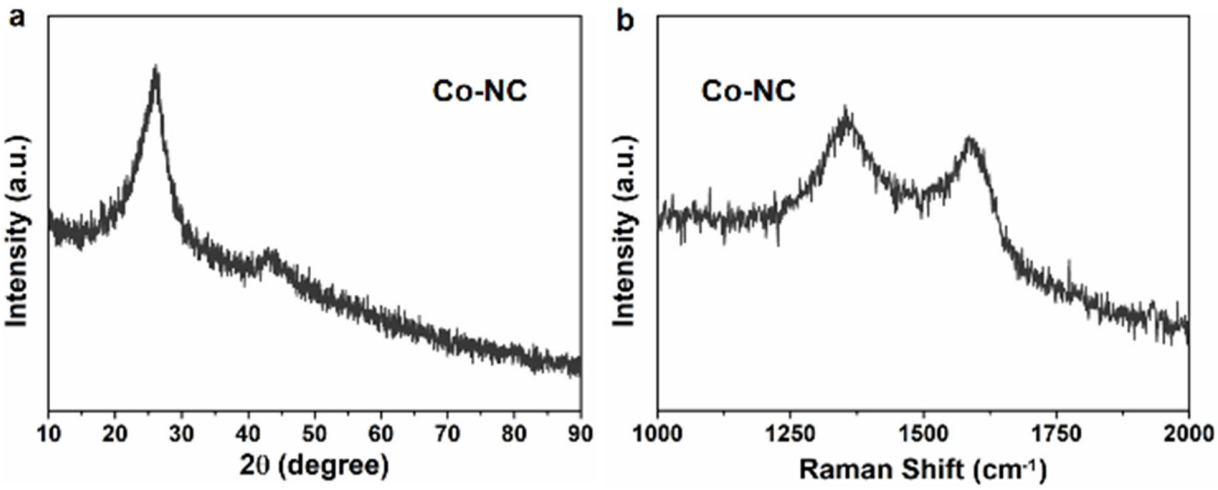

Figure S1. XRD pattern and Raman spectrum of Co-NC.

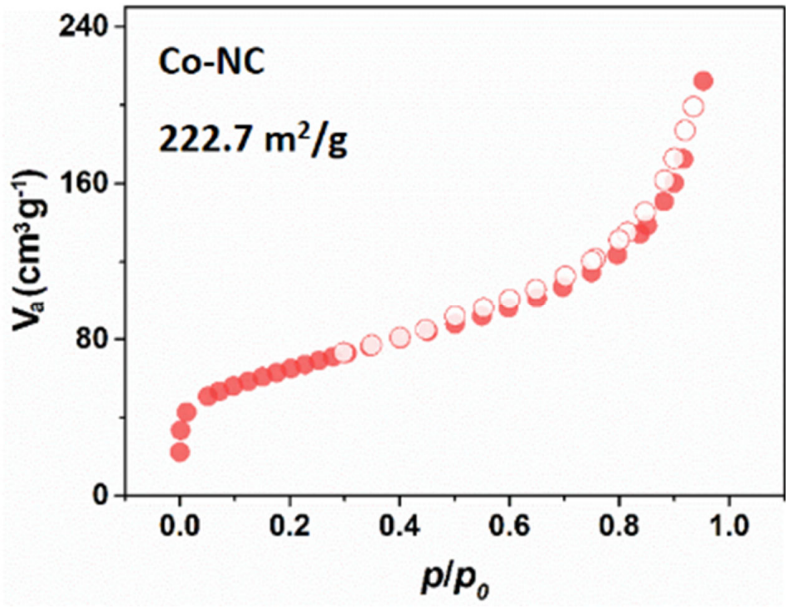

Figure S2. Nitrogen adsorption-desorption isotherms and corresponding BET surface area of Co-NC.

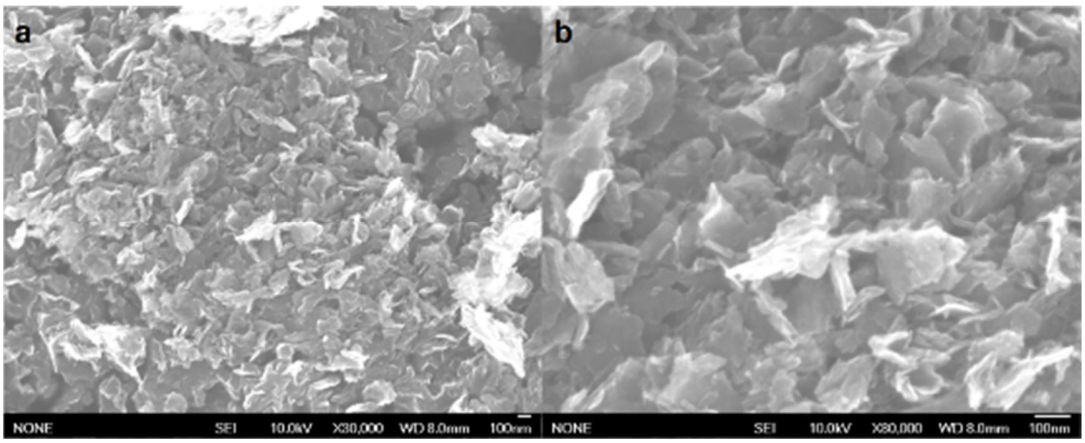

Figure S3. SEM images of Co-NC.

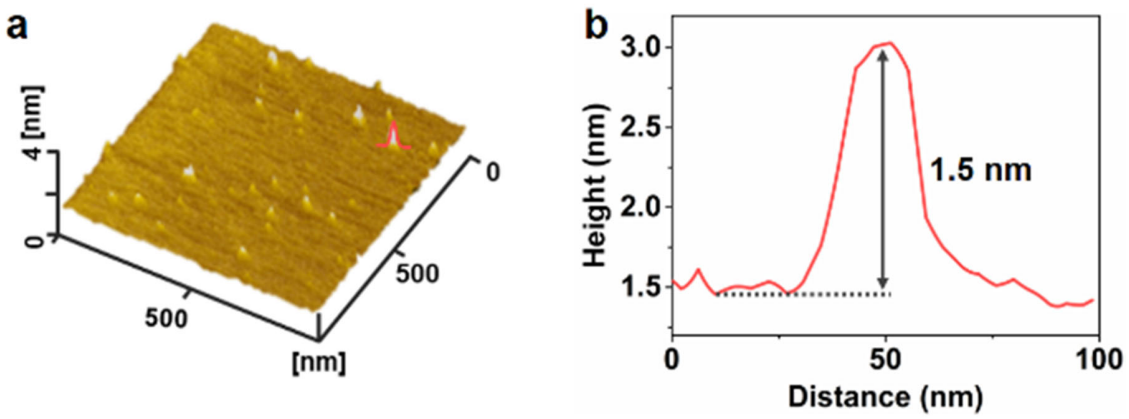

Figure S4. Atomic force microscopy (AFM) image of Co-NC and its typical height profile.

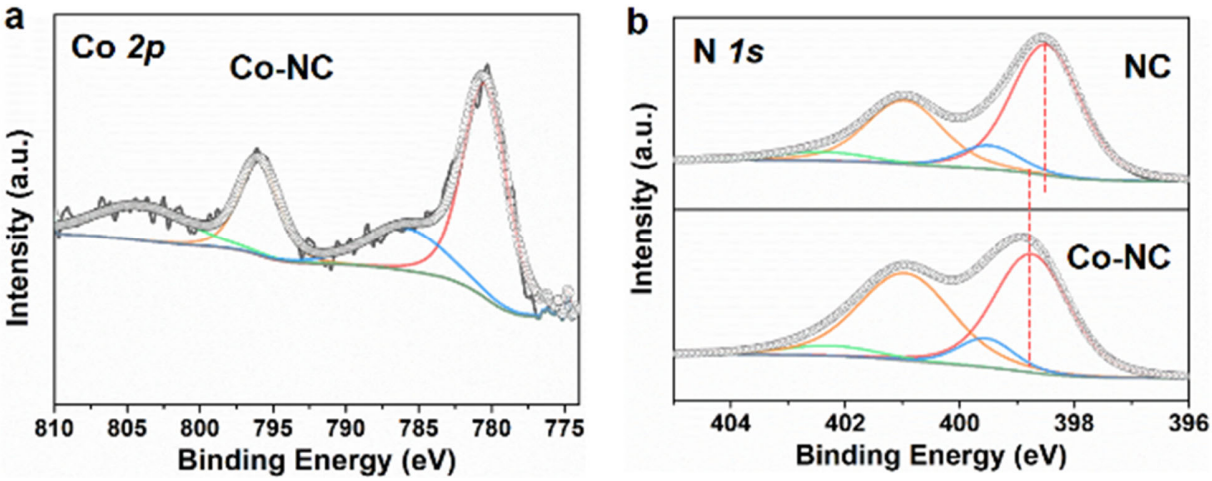

Figure S5. Chemical composition of Co-NC co-catalyst. (a) High-resolution Co *2p* and N *1s* XPS spectra of Co-NC.

Table S1. Structural parameters of Co-NC extracted from the EXAFS fitting.

Sample	Path	CN	*R* (Å)	σ^2 (Å^2)	ΔE_0 (eV)	R factor
Co-NC	**Co-N**	**4**	**1.915**	**0.00804**	**0.585**	**0.01300**

*Reduction factor S_0^2 is 0.706; CN is the coordination number; *R* is interatomic distance (the interatomic length between cobalt site and surrounding N sites); σ^2 is Debye-Waller factor (a measure of thermal and static disorder in absorber-scatter distances); ΔE_0 is edge-energy shift (the difference between the zero kinetic energy value of the sample and that of the theoretical model). R factor is used to value the goodness of the fitting. Definition of *R* factor is a measure of mean square sum of the misfit at each data point.

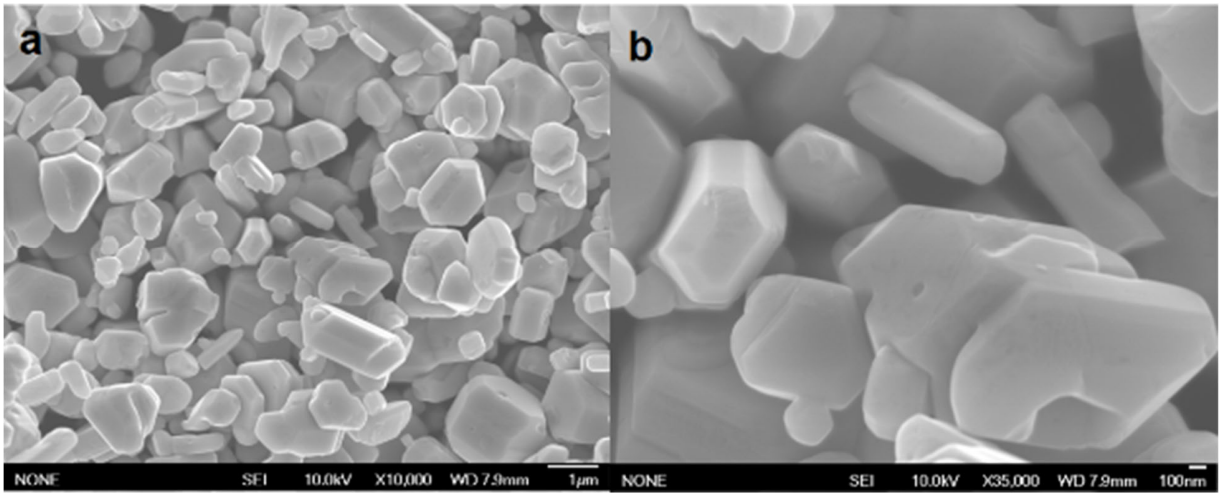

Figure S6. SEM images of bare CdS.

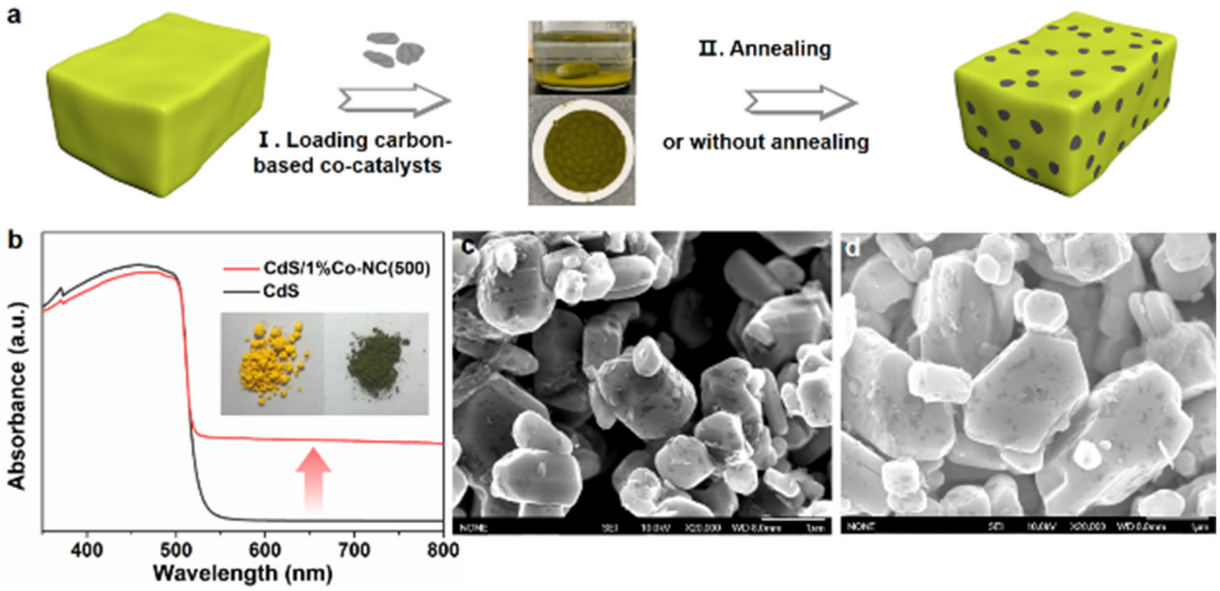

Figure S7. Synthesis and characterizations of CdS/Co-NC. (a) Schematic synthesis process of CdS/co-catalysts. (b) UV−vis spectra of CdS and CdS/Co-NC(500). Inset shows their photographs (left: CdS; right: CdS/Co-NC(500)). (c) SEM images of CdS/Co-NC(500). (d) SEM images of CdS/Co-NC(RT).

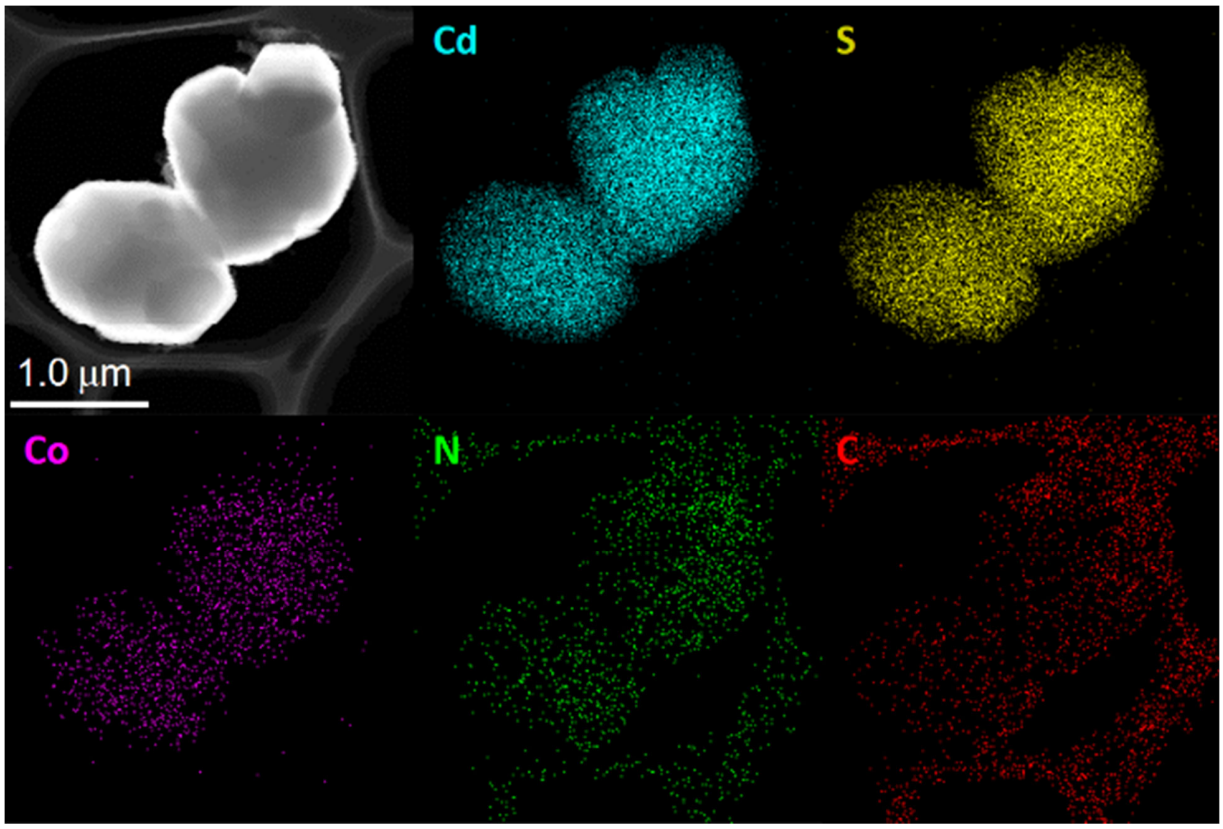

Figure S8. EDS elemental mapping of CdS/1%Co-NC(500).

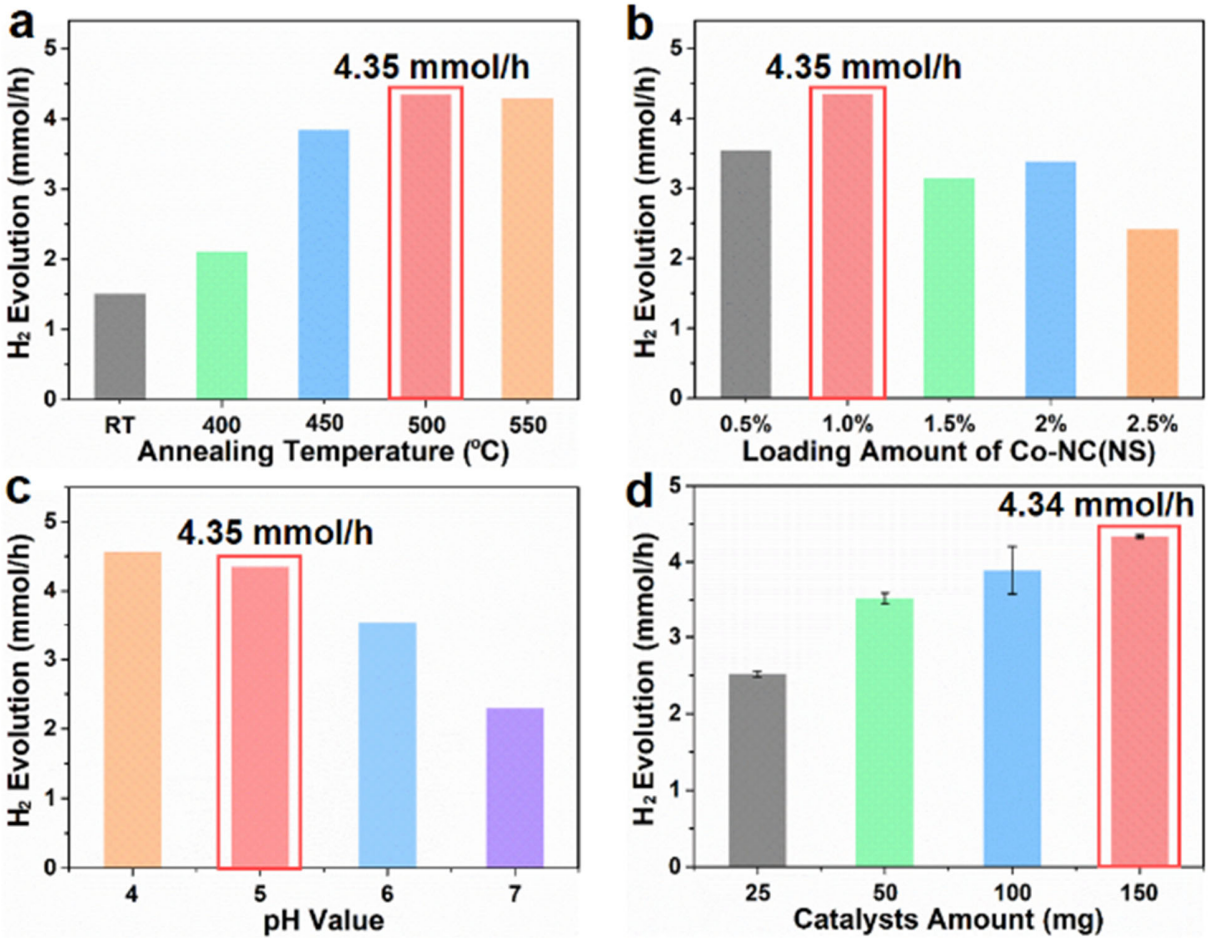

Figure S9. Optimized conditions for CdS/Co-NC. (a) Effect of annealing temperature on H_2 generation activity. (b) Effect of Co-NC loading amount on H_2 generation activity. (c) Effect of pH values of reaction solution on H_2 generation activity. (d) Effect of weight of catalyst CdS/Co-NC(500) on H_2 generation activity.

Table S2. Comparison of various advanced co-catalyst with CdS-based semiconductor for photocatalytic H_2 production.

Co-catalysts	H_2 evolution rate (mmol/h)	Apparent quantum yield	Turnover frequency	Light source	Reaction conditions
Co-NC (this work)	**4.34**	**63.9% at 400 nm; 63.0% at 420 nm**	**16714.7 h^{-1}**	300 W xenon lamp with a L42 filter ($\lambda > 420$ nm)	150 mg catalyst; 20 vol % lactic acid adjusted by NaOH to pH ≈ 5.0
Pd nanoparticles[9]	1.45	11.65 at 420 nm	3148.5 h^{-1}	300 W xenon lamp with a UV-cut filter ($\lambda > 400$ nm)	10 mg catalysts; 0.5 M Na_2S and 0.5 M Na_2SO_3
Pd nanoparticles[9]	0.89	N.A.	1932 h^{-1}	300 W xenon lamp with a UV-cut filter ($\lambda > 400$ nm)	10 mg catalysts; 0.1 M Na_2S and 0.1 M Na_2SO_3
Pt nanoparticles[10]	1.68	33.0% at 420 nm	81.9 h^{-1}	300 W xenon lamp with a UV-cut filter ($\lambda > 420$ nm)	100 mg catalysts; 0.25 M Na_2SO_3 and 0.35 M Na_2S
Single Pt atom[11]	0.99	N.A.	1428.6 h^{-1}	300 W xenon lamp with a UV-cut filter ($\lambda > 420$ nm)	50 mg catalyst; 20 vol % lactic acid (pH = 2.1)
Single Pt atom[11]	2.37	N.A.	943.85 h^{-1}	300 W xenon lamp with a UV-cut filter ($\lambda > 420$ nm)	50 mg catalyst; 20 vol % lactic acid (pH = 2.1)
2D-CoS_2[12]	0.55	10.2% at 420 nm	16.9 h^{-1}	A full spectrum solar simulator (CEL-S500) with AM 1.5G filter	100 mg catalyst; 20 vol % 0.75 M ascorbic acid
Co_9S_8[13]	0.02	N. A.	-	300 W xenon lamp with an AM 1.5 air mass filter ($\lambda > 400$ nm)	20 mg catalyst; Na_2S and Na_2SO_3
CoP[14]	0.001	N.A.	0.4 h^{-1}	A white LED light source (30×3 W, $\lambda > 420$ nm)	5 mg catalyst; pure water
CoE-300[15]	3.65	N.A.	600 h^{-1}	300 W xenon lamp with a cut-off filter ($\lambda > 420$ nm)	100 mg; 30 vol % lactic acid adjusted by NaOH to pH ≈ 5.0
NiE-350[15]	5.0	78.4% at 420 nm	864 h^{-1}	300 W xenon lamp with a cut-off filter ($\lambda > 420$ nm)	100 mg; 30 vol % lactic acid adjusted by NaOH to pH ≈ 4.5
Ti_3C_2[16]	0.29	40.1 % at 420 nm	-	300 W xenon lamp with a UV-cut filter ($\lambda > 420$ nm);	20 mg catalyst; 22 vol % lactic acid
MoO_x clusters[17]	0.57	13.4% at 420 nm	32.0 h^{-1}	300 W xenon lamp with a UV-cut filter	200 mg catalyst; 20 vol % lactic acid (pH = 2.1)

Single-layer WS_2[18]	0.02	N. A.	-	300 W Xe lamp with a UV-cut filter ($\lambda > 420$ nm)	10 mg catalyst; 10 vol% lactic aqueous solution
Monolayer 2H-MoS_2[19]	4.84	62.1% at 420 nm	-	300 W xenon lamp with a L42 filter ($\lambda > 420$ nm)	100 mg catalyst; 20 vol % lactic acid adjusted by NaOH to pH ≈ 5.0
MoS_2[20]	0.18	54% at 420 nm	-	300 W xenon lamp with a UV-cut filter ($\lambda > 400$ nm)	20 mg catalyst; 10 vol % lactic acid
MoS_2/graphene[21]	1.8	28.1% at 420 nm	-	300 W xenon lamp with a L42 filter ($\lambda > 420$ nm)	20 mg catalyst; 20 vol % lactic acid
Single-layer MoS_2[22]	2.59	38.4% at 420 nm	-	300 W xenon lamp with a L42 filter ($\lambda > 420$ nm)	200 mg catalyst; 20 vol % lactic acid
Poorly crystalline MoS_2 monolayer[23]	5.5	71.6% at 420 nm	-	300 W xenon lamp with a L42 filter ($\lambda > 420$ nm)	200 mg catalyst; 20 vol % lactic acid adjusted by NaOH to pH ≈ 5.0
Cobalt substituted MoS_2 monolayer with poor crystallinity[24]	6.2	80.2 at 420 nm	-	300 W xenon lamp with a L42 filter ($\lambda > 420$ nm)	200 mg catalyst; 20 vol % lactic acid adjusted by NaOH to pH ≈ 5.0

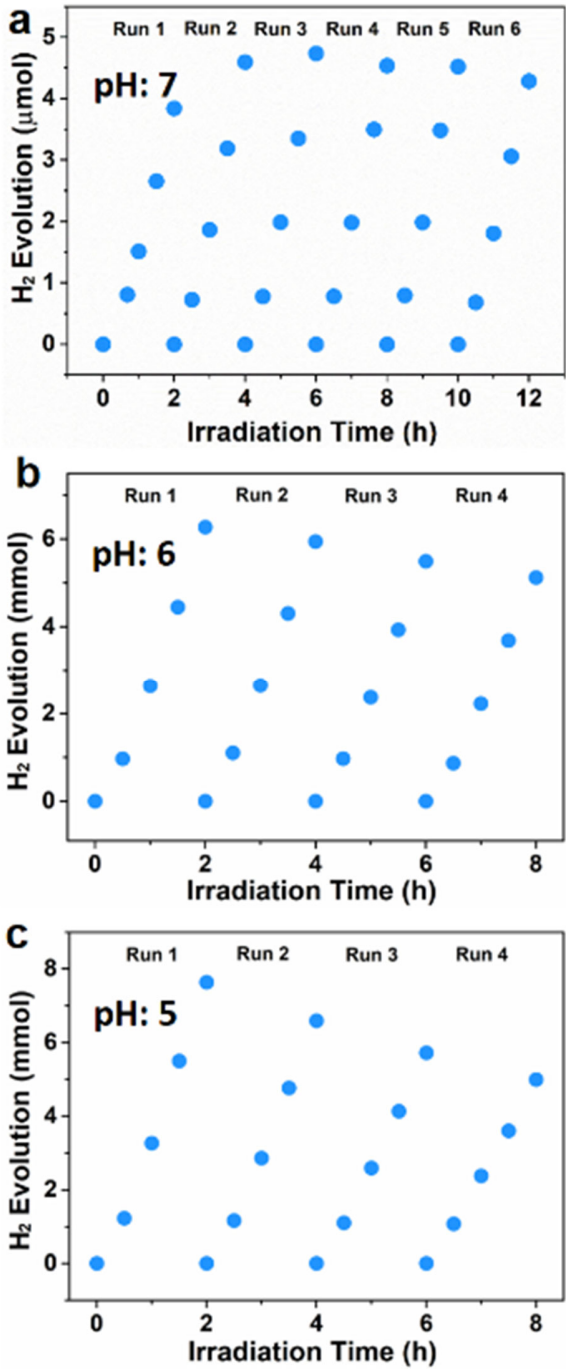

Figure S10. Stability of H_2 generation for CdS/Co-NC(500) over several runs at different pH values.

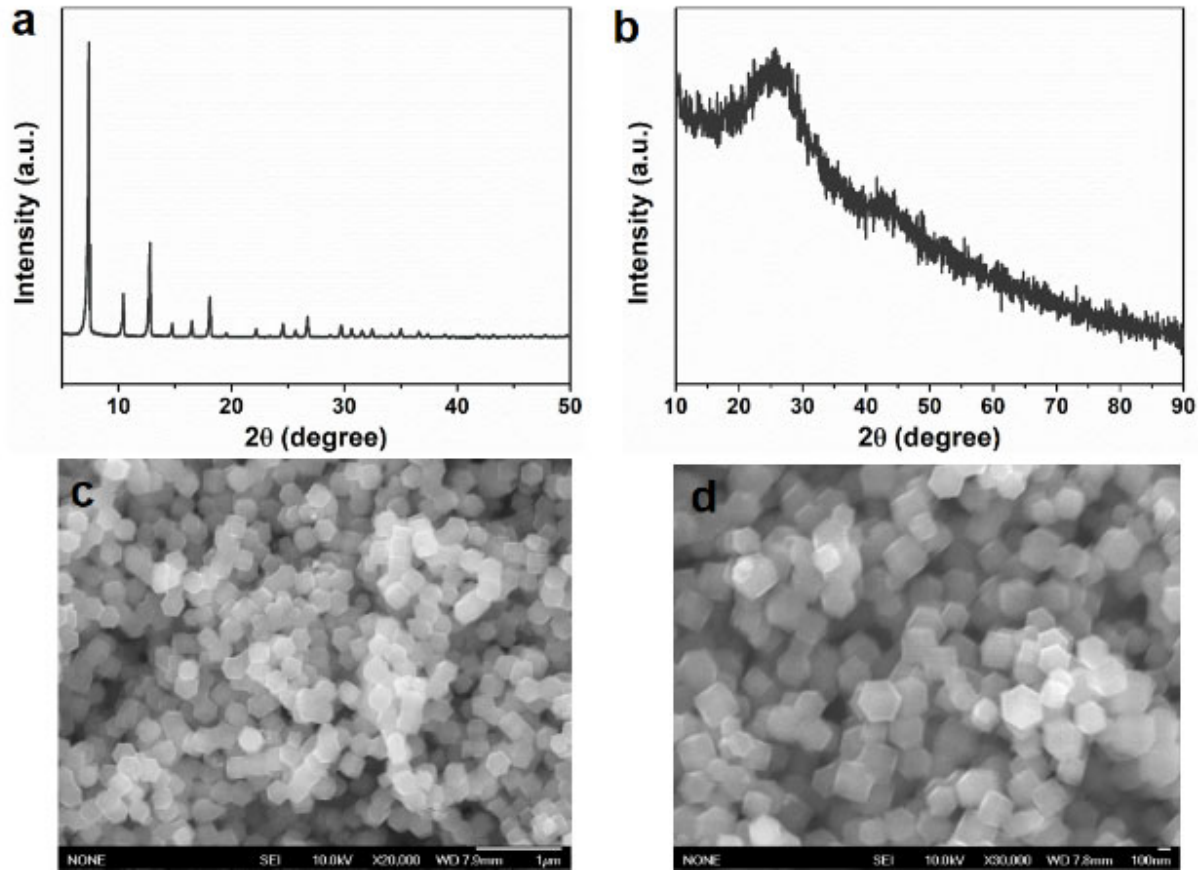

Figure S11. Characterizations of Co-NC_{rd}. (a) XRD pattern of Co-incorporated ZIF-8 (precursor of Co-NC_{rd}). (b) XRD pattern of Co-NC_{rd}. (c) and (d) SEM images of Co-NC_{rd}.

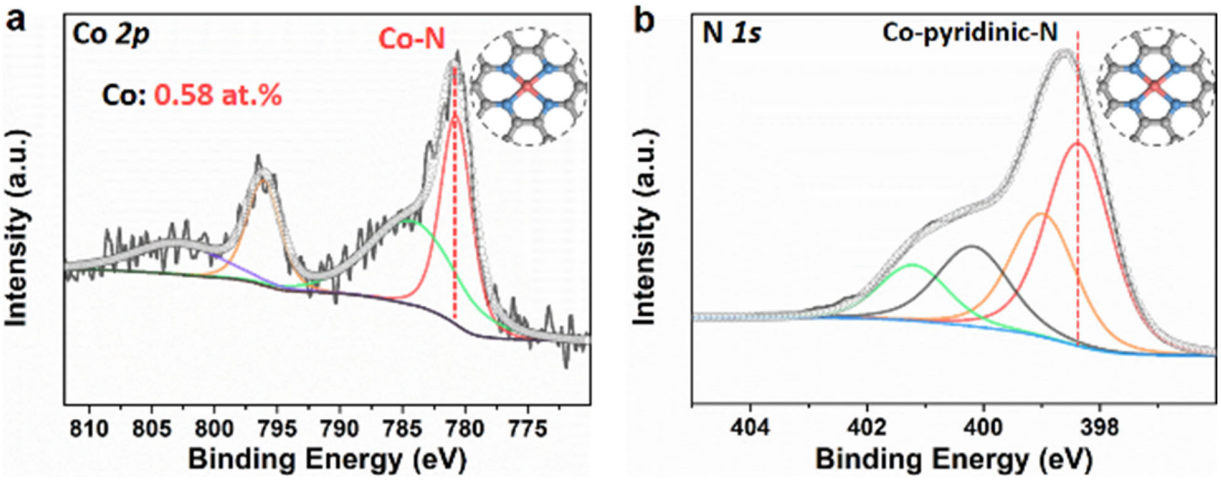

Figure S12. High-resolution Co *2p* (a) and N *1s* (b) XPS spectra of Co-NC_{rd}.

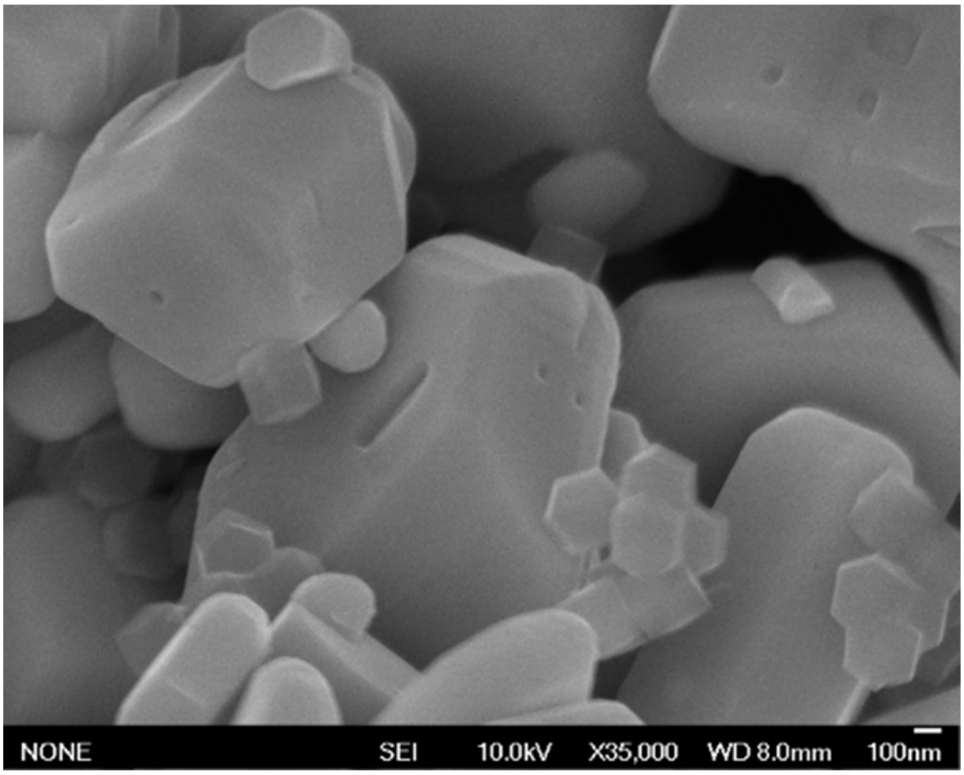

Figure S13. SEM image of CdS/1%Co-NC_{rd}(500).

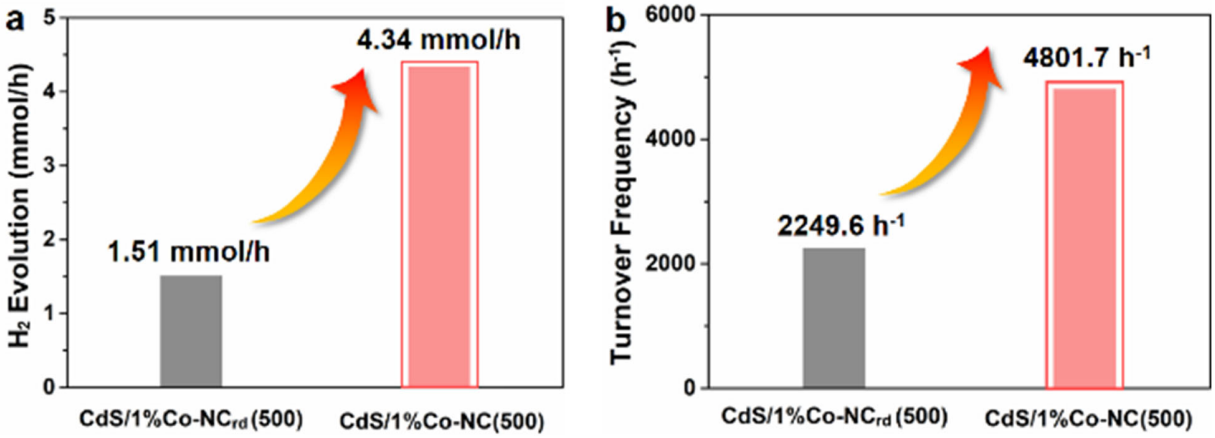

Figure S14. Comparison of H_2 generation and TOF of CdS/Co-NC(500) and CdS/Co-NC_{rd}(500).

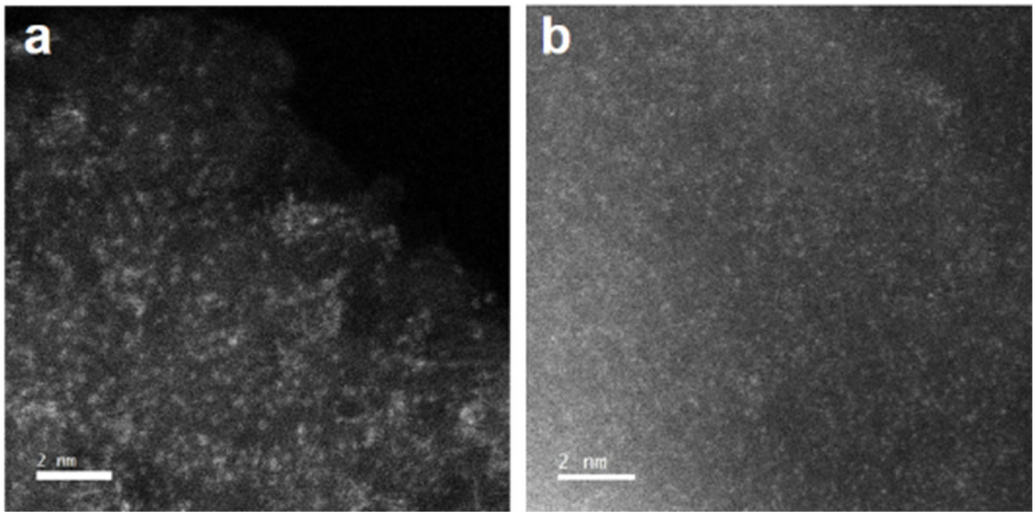

Figure S15. Aberration-corrected HAADF-STEM images of (a) Fe-NC and (b) Ni-NC.

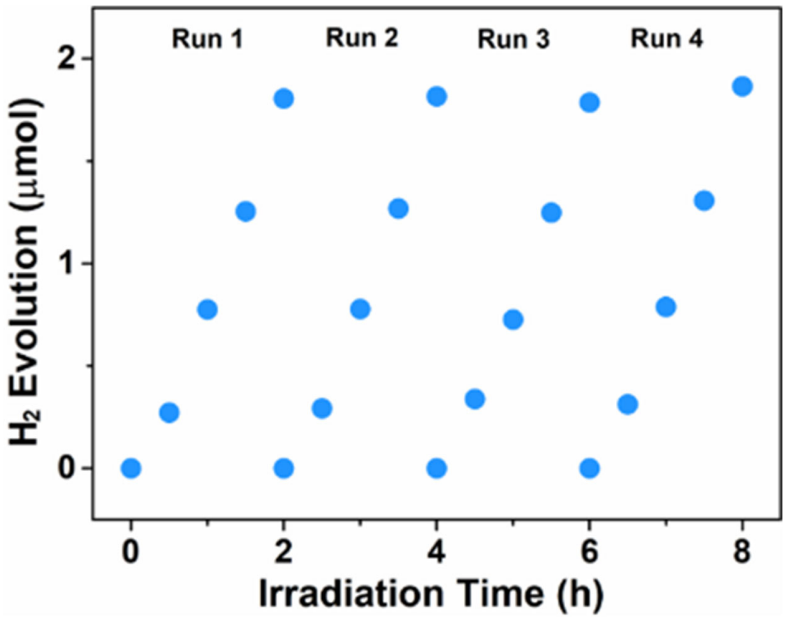

Figure S16. Stability of H_2 generation for CdS/1%NC(500) over several runs with a pH of 5.

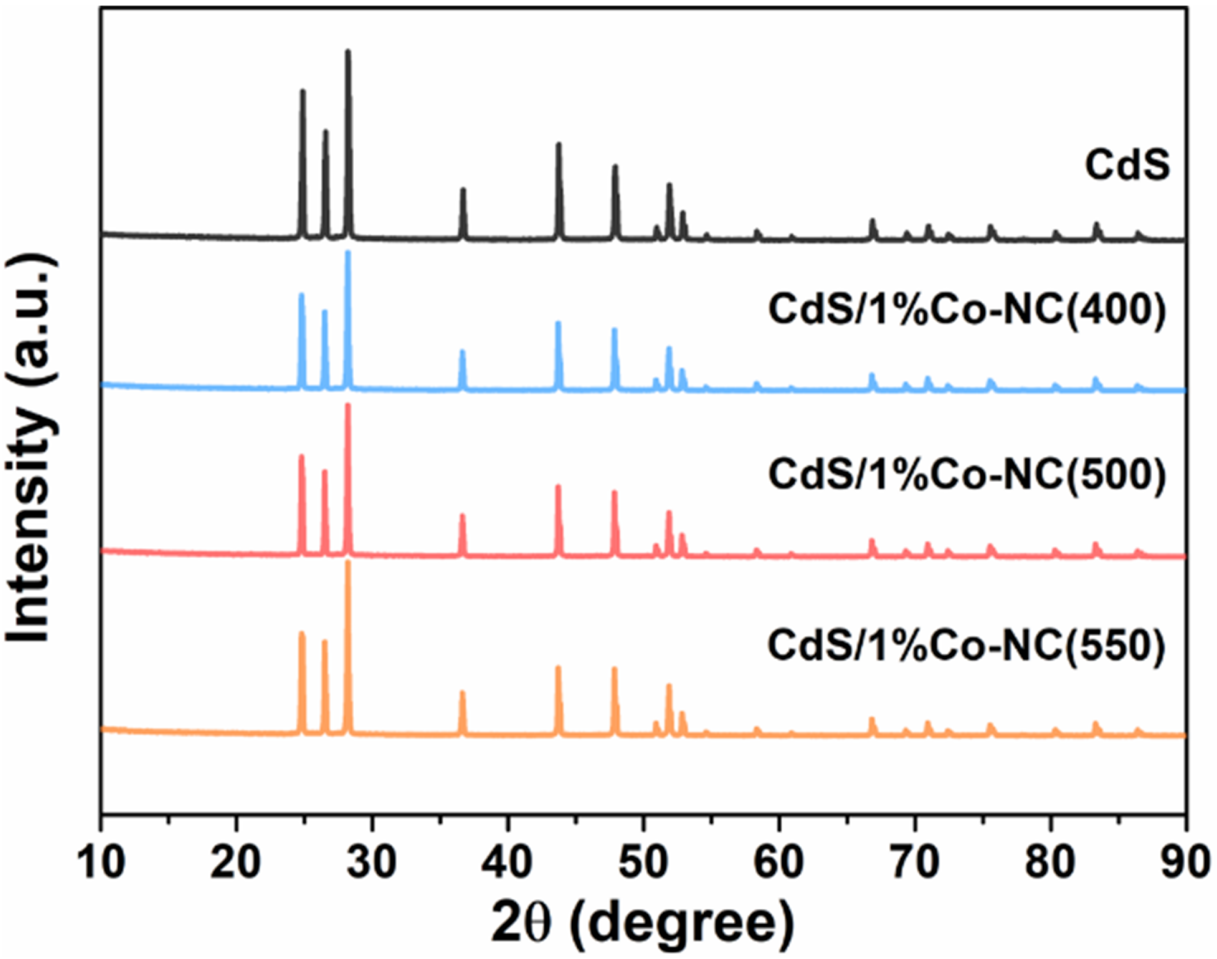

Figure S17. XRD patterns of pure and CdS/Co-NC annealed at different temperatures.

Table S3. The lattice parameters (unit: Å) for CC, NC and Fe-NC model.

model	a	b	c
CC	12.32	12.32	12.00
NC	12.30	12.30	12.00
Fe-NC	12.21	12.21	12.00

Table S4. The adsorption free energy of H on different site of surface, including C, N, and metal (M) site.

model	C-H	N-H	M-H
CC	1.69	-	-
NC	1.38	2.09	-
Fe-NC	1.68	1.69	0.85
Ni-NC	1.68	1.49	1.79
Co-NC	2.18	-	0.53
NC_{vac}	1.66	-2.15	-

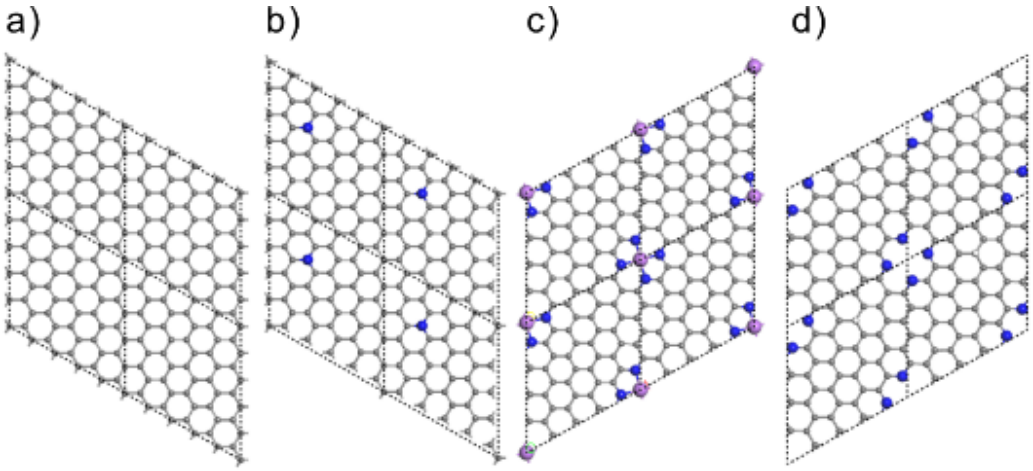

Figure S18. The optimized structure of different model. (a) CC, (b) NC, (c) M-NC(M = Fe, Co, Ni) and (d) NC_{vac} model. The purple, blue, grey and white ball represent the Metal, N, C and H atom, respectively.

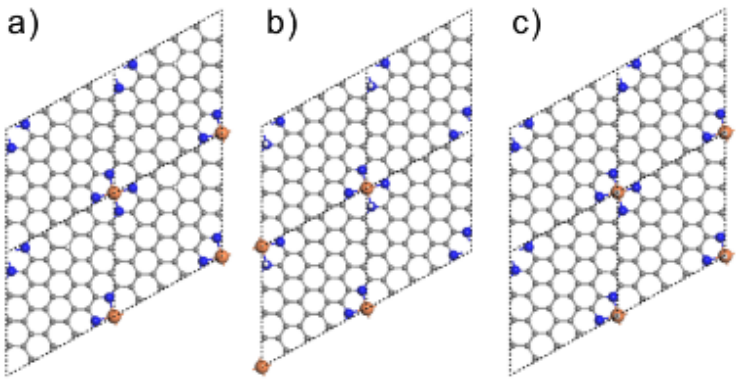

Figure S19. The structure of H adsorbed on different site of Fe-NC. (a) C site, (b) N site and (c) Fe site. The orange, blue, grey and white ball represent the Fe, N, C and H atom, respectively.

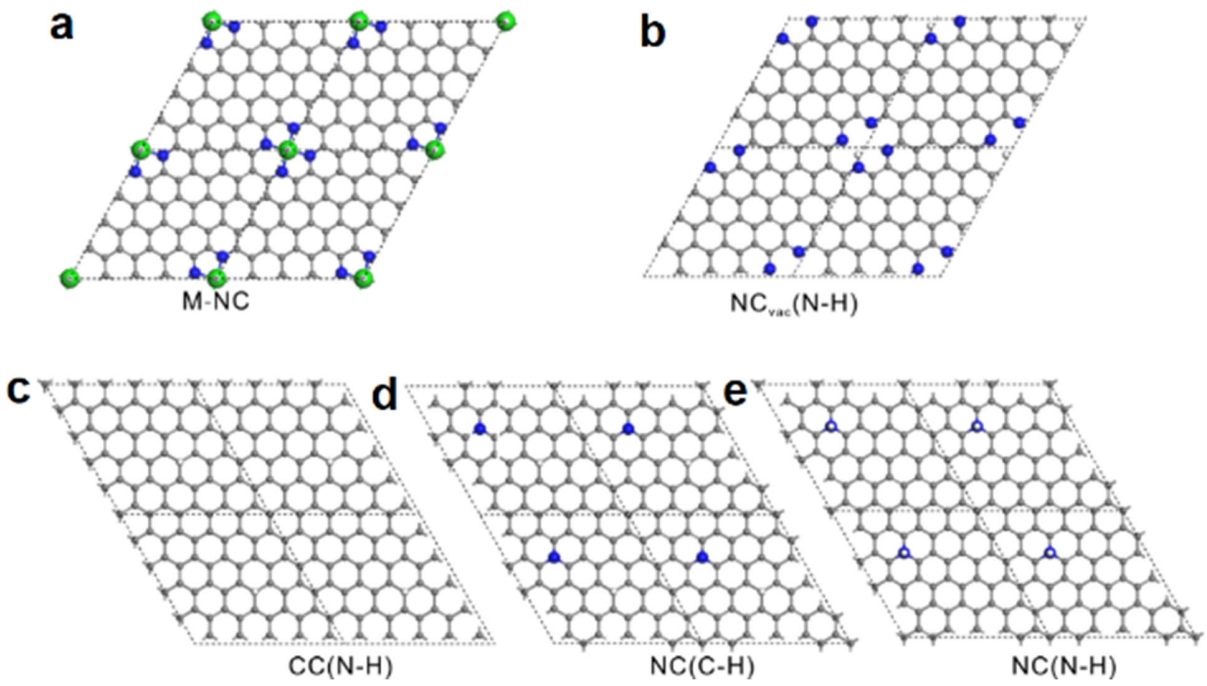

Figure S20. The calculated sites for hydrogen adsorption.

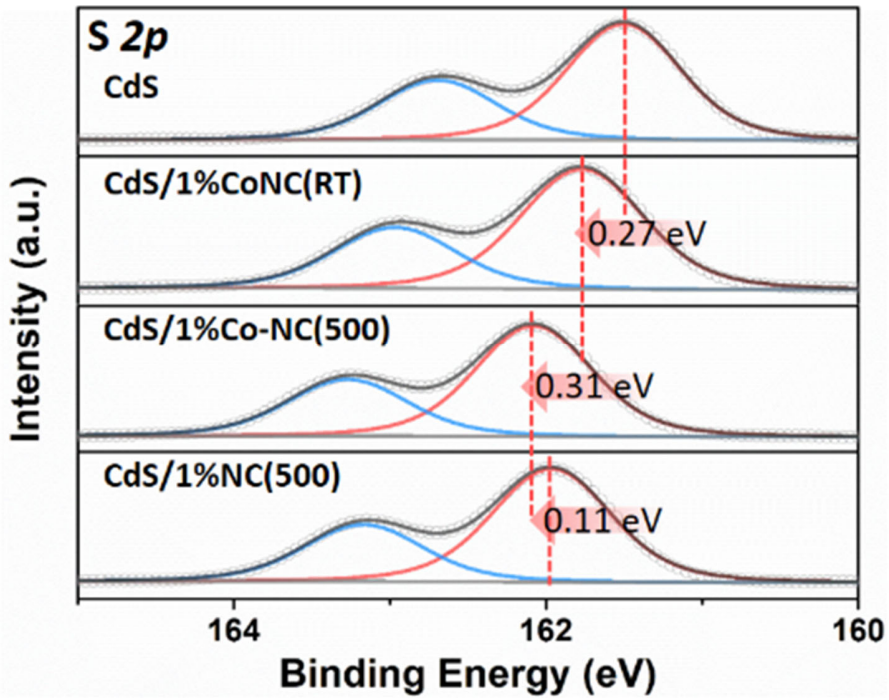

Figure S21. High-resolution S *2p* XPS spectra of samples.

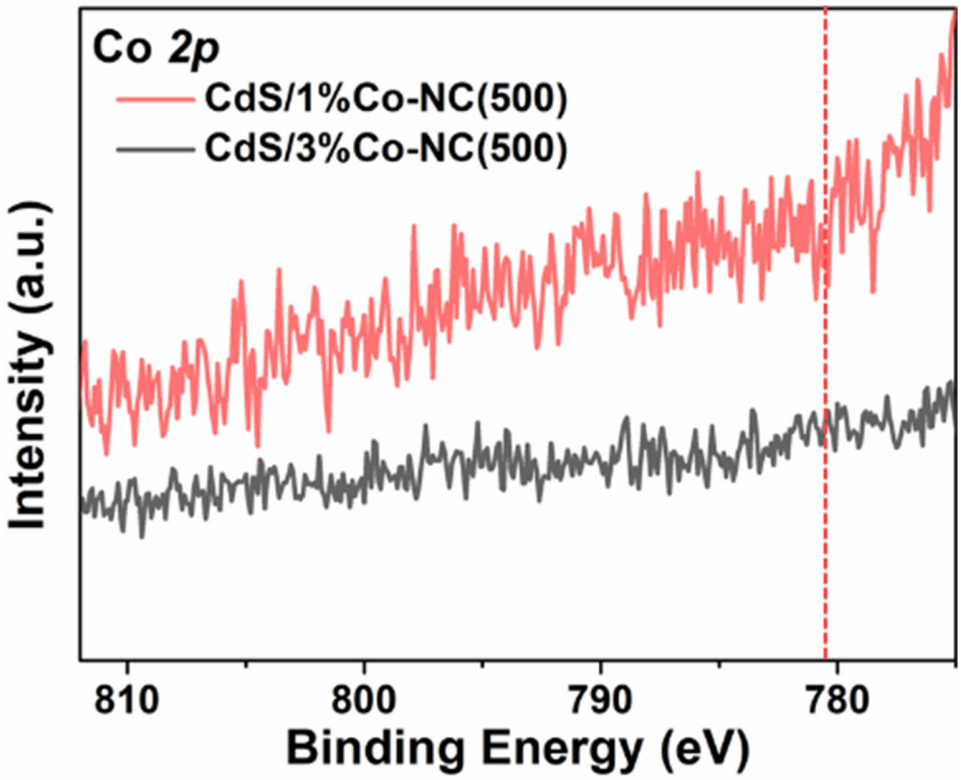

Figure S22. High-resolution Co *2p* XPS spectra of CdS/1%Co-NC(500).

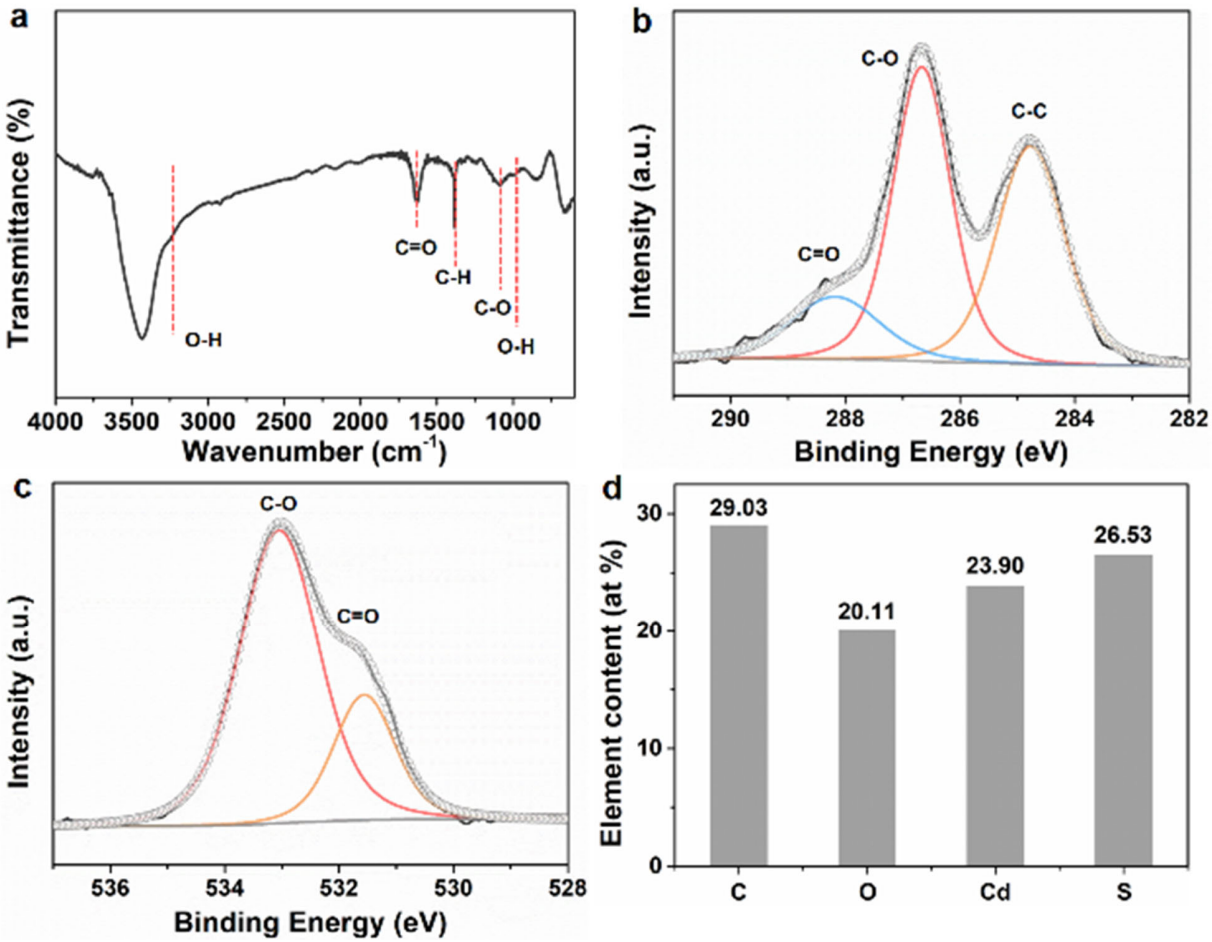

Figure S23. Identification of abundant surface adventitious carbon on commercial CdS. (a) FT-IR spectrum. Note: the signals marked with red dash lines refer to the species in adventitious carbon on the surfaces of bare CdS. (b) High-resolution C *1s* and (c) O *1s* spectra. (d) Element content.

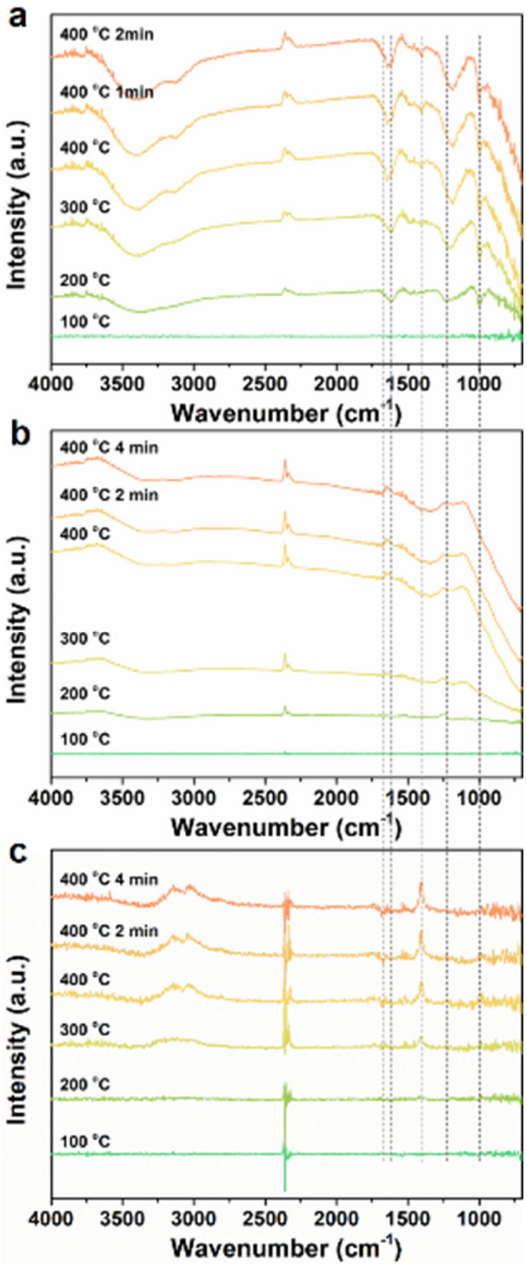

Figure S24. In situ FT-IR spectra of CdS/Co-NC(RT) (a), pure CdS (b) and Co-NC (c) measured at increased temperature.

Noting that most of surface region of CdS in CdS/Co-NC(RT) hybrid is uncovered with Co-NC (refer to the SEM image of annealed hybrid provided in Figure S7c) and such areas are comparable to those of pristine CdS (Figure S6); similarly, the outward-facing surfaces of Co-NC in CdS/Co-NC should be same as those of pure Co-NC. Considering these two points, it's supposed to observe similar FT-IR signals for CdS, Co-NC and CdS/Co-NC(RT). Unexpectedly, the CdS/Co-NC(RT) exhibits different signals, especially those at ~1000 and 1626 cm^{-1}, relative to pure CdS and Co-NC under identical conditions (Figure S24). This distinction indicates that, in CdS/Co-NC(RT), most of those reduced C=O, C-O and OH groups originate from the decomposition of adventitious hydrocarbon confined at the interfaces between CdS and Co-NC rather than on the naked surfaces of CdS and Co-NC.

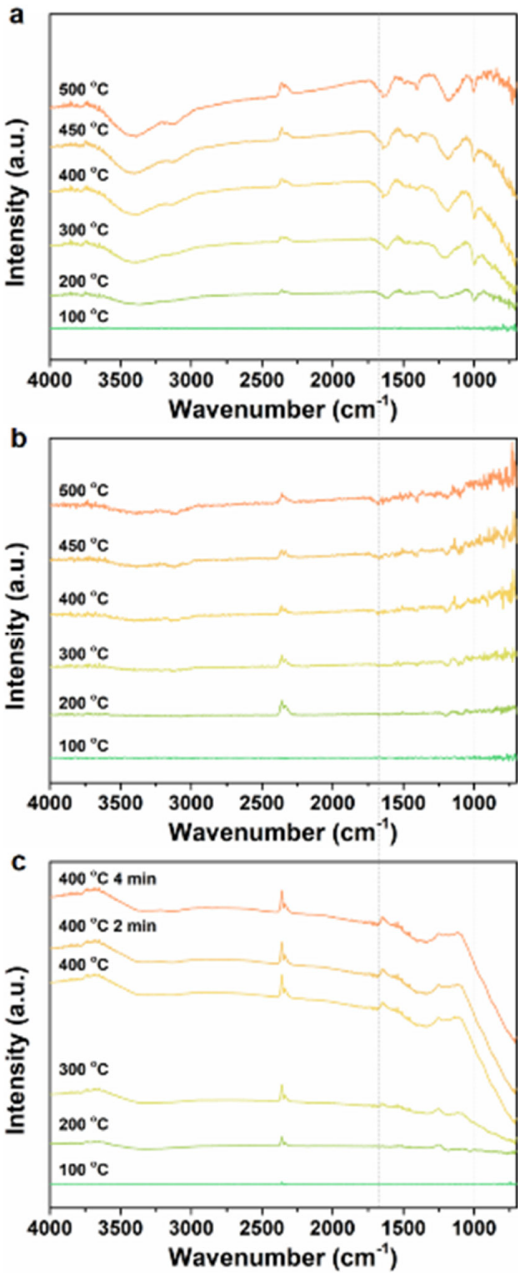

Figure S25. In situ FT-IR spectra of CdS/Co-NC(RT) (a), CdS/Co-NC(500) (b) and pure CdS (c) measured at increased temperature.

A weak declined signal at ~1676 cm^{-1} (C=O) appears for CdS/Co-NC(500), which is same as that of bare CdS but different from that of CdS/Co-NC(RT) locating at ~1626 cm^{-1} (Figure S25). Besides that, the CdS/Co-NC(500) and bare CdS show negligible signal at ~1000 cm^{-1} while CdS/Co-NC(RT) delivers obvious declined signal this location. This contrast experiment confirms that CdS/Co-NC(500) possesses negligible interfacial carbon species because of the pre-annealing process but some readsorbed carbon species on its' surface.

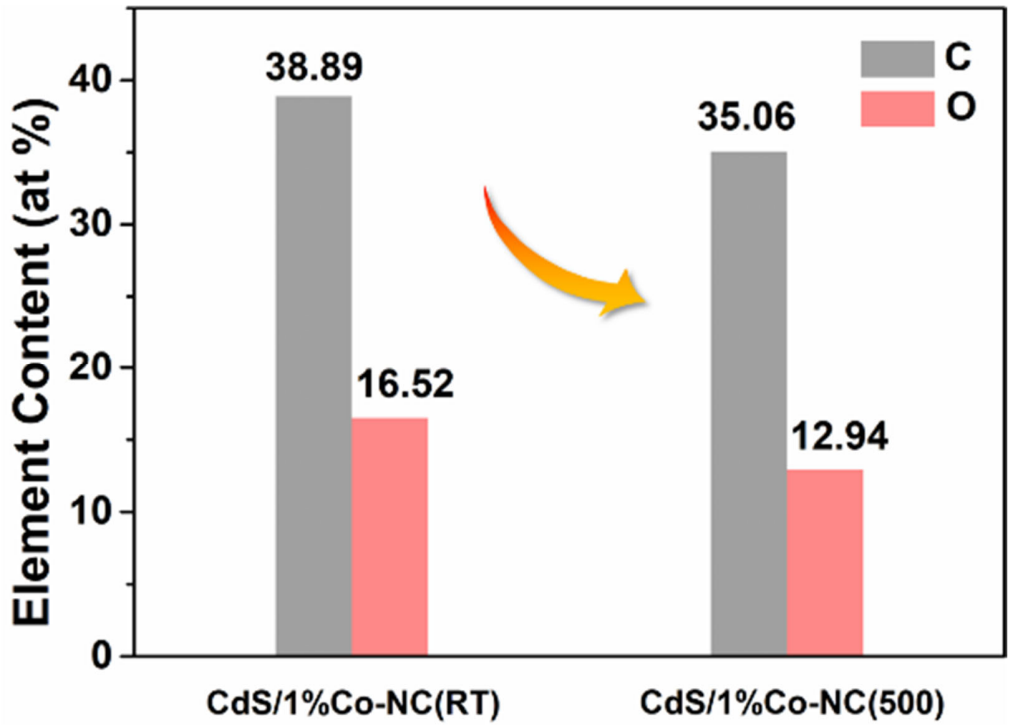

Figure S26. Element content change of CdS/Co-NC before and after annealing.

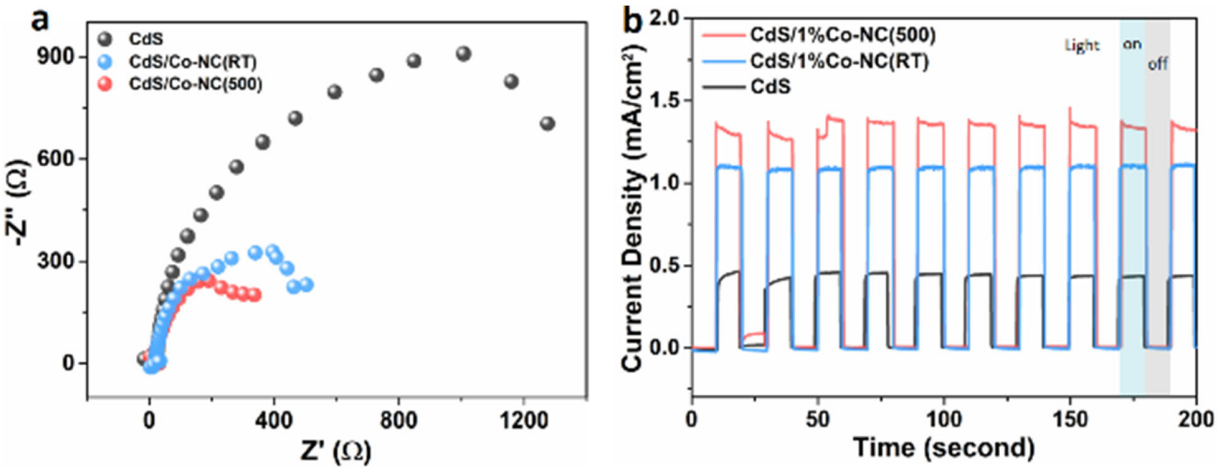

Figure S27. Photoelectrochemical characterizations of a group of samples. (a) Electrochemical impedance spectroscopy (EIS) Nyquist plots under irradiation condition. (b) Periodic on/off photocurrent response under visible-light irradiation.

Reference

[1] G. Kresse, J. Hafner, Physical Review B, 47 (1993) 558-561.

[2] G. Kresse, J. Furthmüller, Physical Review B, 54 (1996) 11169-11186.

[3] J.P. Perdew, K. Burke, M. Ernzerhof, Physical Review Letters, 77 (1996) 3865-3868.

[4] P.E. Blöchl, Physical Review B, 50 (1994) 17953-17979.

[5] G. Kresse, D. Joubert, Physical Review B, 59 (1999) 1758-1775.

[6] Q.-K. Li, X.-F. Li, G. Zhang, J. Jiang, Journal of the American Chemical Society, 140 (2018) 15149-15152.

[7] H. Xu, D. Cheng, D. Cao, X.C. Zeng, Nature Catalysis, 1 (2018) 339-348.

[8] P. Wang, S.N. Steinmann, G. Fu, C. Michel, P. Sautet, ACS Catalysis, 7 (2017) 1955-1959.

[9] Q. Sun, N. Wang, J. Yu, J.C. Yu, Adv. Mater., 30 (2018) e1804368.

[10] L. Shang, B. Tong, H. Yu, G.I.N. Waterhouse, C. Zhou, Y. Zhao, M. Tahir, L.-Z. Wu, C.-H. Tung, T. Zhang, Advanced Energy Materials, 6 (2016).

[11] X. Wu, H. Zhang, J. Dong, M. Qiu, J. Kong, Y. Zhang, Y. Li, G. Xu, J. Zhang, J. Ye, Nano Energy, 45 (2018) 109-117.

[12] P. Wang, Y. Mao, L. Li, Z. Shen, X. Luo, K. Wu, P. An, H. Wang, L. Su, Y. Li, S. Zhan, Angew. Chem. Int. Ed. Engl., (2019).

[13] B. Qiu, Q. Zhu, M. Du, L. Fan, M. Xing, J. Zhang, Angew. Chem. Int. Ed. Engl., 56 (2017) 2684-2688.

[14] R. Shi, H.F. Ye, F. Liang, Z. Wang, K. Li, Y. Weng, Z. Lin, W.F. Fu, C.M. Che, Y. Chen, Adv. Mater., 30 (2018).

[15] G. Zhao, Y. Sun, W. Zhou, X. Wang, K. Chang, G. Liu, H. Liu, T. Kako, J. Ye, Adv. Mater., 29 (2017) 1703258.

[16] J. Ran, G. Gao, F.T. Li, T.Y. Ma, A. Du, S.Z. Qiao, Nat. Commun., 8 (2017) 13907.

[17] H. Zhang, P. Zhang, M. Qiu, J. Dong, Y. Zhang, X.W.D. Lou, Adv. Mater., 31 (2019) e1804883.

[18] J. Chen, X.J. Wu, L. Yin, B. Li, X. Hong, Z. Fan, B. Chen, C. Xue, H. Zhang, Angew. Chem. Int. Ed. Engl., 54 (2015) 1210-1214.

[19] K. Chang, X. Hai, H. Pang, H. Zhang, L. Shi, G. Liu, H. Liu, G. Zhao, M. Li, J. Ye, Adv. Mater., 28 (2016) 10033-10041.

[20] B. Sun, W. Zhou, H. Li, L. Ren, P. Qiao, W. Li, H. Fu, Adv. Mater., 30 (2018) e1804282.

[21] K. Chang, Z. Mei, T. Wang, Q. Kang, S. Ouyang, J. Ye, ACS Nano, 8 (2014) 7078-7087.

[22] K. Chang, M. Li, T. Wang, S. Ouyang, P. Li, L. Liu, J. Ye, Advanced Energy Materials, 5 (2015).

[23] X. Hai, W. Zhou, K. Chang, H. Pang, H. Liu, L. Shi, F. Ichihara, J. Ye, J. Mater. Chem. A, 5 (2017) 8591-8598.

[24] X. Hai, W. Zhou, S. Wang, H. Pang, K. Chang, F. Ichihara, J. Ye, Nano Energy, 39 (2017) 409-417.